ANNALS OF GEOPHYSICS, 68, 1, V103, 2025; doi:10.4401/ag-9158
OPEN ACCESS

Dynamics and hazards of pyroclastic avalanches at Etna volcano (Italy)

Francesco Zuccarello[*,1], Mattia de' Michieli Vitturi[2], Tomaso Esposti Ongaro[2], Gaetana Ganci[1], Daniele Andronico[1], Stefano Branca[1], Annalisa Cappello[1]

(1) Istituto Nazionale di Geofisica e Vulcanologia, Osservatorio Etneo – Sezione di Catania, Catania, Italy
(2) Istituto Nazionale di Geofisica e Vulcanologia, Sezione di Pisa, Pisa, Italy

Article history: received September 16, 2024; accepted January 23, 2025

Abstract

We present a multidisciplinary research aimed at quantifying the conditional probabilities for hazards associated with pyroclastic avalanches at Etna, which combines physical and numerical modeling of granular avalanches and probabilistic analysis. Pyroclastic avalanches are modeled using the depth-averaged model IMEX-SfloW2D, which is able to simulate the transient propagation and emplacement of granular flows generated by the collapse of a prescribed volume of granular material. Preliminary sensitivity analysis allowed us to identify the main controlling parameters of the dynamics, i.e. the total avalanche mass, the initial position of the collapsing granular mass (and the associated terrain morphology), the initial avalanche velocity, and the two rheological parameters which determine the mechanical properties of the flow. While the first two parameters can be considered as "scenario parameters" in the definition of the hazards, the initial velocity and the rheological parameters need to be calibrated. We therefore adopted a methodology for the statistical calibration of the physical model parameters based on field observations. We used data from the pyroclastic avalanche that occurred on February 10, 2022 at Etna, for which we had an accurate mapping of the deposit and some estimates of the total mass and the initial volume. We then run a preliminary ensemble of numerical simulations, with fixed initial volume and position, to calibrate the other input parameters. Based on the accuracy of the matching of the simulated and observed deposits (measured by the Jaccard Index), we extracted from the simulation ensemble a subsample of equally probable combinations of initial velocities and rheological parameters. We then built an ensemble of model input parameters, with varying (i) avalanche volumes, (ii) initial positions, (iii) velocity, and (iv) rheological coefficients. The initial volume range was chosen within the range of observed pyroclastic avalanches at Etna (i.e., between 0.1 and 3×10^6 m^3), using a prescribed probability distribution extracted from the literature data. The initial positions have been chosen on the flanks of the South East Crater of Etna, with homogeneous spatial distribution. The initial velocity and the rheological coefficients were chosen from the subsample created with the calibration. Finally, a semi-automatic procedure (digital workflow) running the Monte Carlo simulation allowed us to produce the first probabilistic map of pyroclastic avalanche invasion at Etna. Such a map, conditional to the occurrence of a pyroclastic avalanche event, can be used to identify the hazardous areas of the volcano and to plan mitigation measures.

Keywords: Mt. Etna; Pyroclastic Avalanche; Numerical Simulation; Parameters Calibration; Hazard Map

1. Introduction

One of the most hazardous phenomena in volcanic areas are pyroclastic density currents (PDCs), which are hot flows composed of pyroclastic fragments of different sizes, lithic fragments, and fluid that spread rapidly along the slopes of the volcanic edifices (Druitt, 1992; Wilson and Houghton, 2000). They are gravity-driven flows, characterized by negative buoyancy with respect to the atmosphere that show a large spectrum of flows regimes, from dilute transport (volume fraction of solid material <0.001) to high particle-concentration flows (volume fraction of particles >0.1) (Esposti Ongaro et al., 2020). In case of PDCs characterized by high-particle-concentration, the motion is driven mainly by the longitudinal (i.e., parallel to the ground) component of gravity and stops when either the slope is reduced or their momentum is dissipated by friction. Flows dominated by the high-concentrated regime generated by the collapse of lava domes or scoria cones are generally characterized by relatively small volumes of volcanic materials (less than $\sim 10 \times 10^6$ m^3) and thin layers, and their motion is confined within the volcanic slopes and controlled by the topography (de' Michieli Vitturi et al., 2019). These types of flows can be referred to as pyroclastic avalanches, since they present similar dynamics to other granular flows, such as landslide and snow avalanches (Mcewen and Malin, 1989; Pudasaini and Hutter, 2007). While pyroclastic avalanches share physical similarities with PDCs, the term "avalanche" specifically highlights their gravity-dominated dynamics. PDCs, by contrast, are primarily driven by density contrasts with the atmosphere, often exhibiting broader lateral spreading beyond the slopes.

The difficulty of predicting their occurrence and fast development (in the order of minutes) makes pyroclastic avalanches one of the major sources of hazard in active basaltic volcanoes with persistent eruptive activity, where the continuous accumulation of volcanic materials on steep slopes, with inclination similar or greater than their natural angle of repose, poses favorable conditions for the generation of pyroclastic avalanches (e.g., Behncke, 2009; Di Roberto et al., 2014; Andronico et al., 2018; Calvari et al., 2020; Risica et al., 2022; Charbonnier et al., 2023).

At Mt. Etna volcano (Italy), the frequency of pyroclastic avalanches has increased in the last decades. They are commonly observed at summit craters, especially at the South East Crater (SEC) during paroxysmal eruptions, which are characterized by energetic lava fountains, high-rate of lava effusion and formation of pyroclastic columns high several kilometers (e.g., Andronico et al., 2021 and references therein). Pyroclastic avalanches have also been emplaced during episodes of low to intermediate Strombolian activity and lava effusion at the SEC, which occurred after a sequence of paroxysmal eruptions (e.g., February 11, 2014 and May 21, 2022; Andronico et al., 2018; INGV-OE, 2022a). Generally, they are generated by the partial collapse of the proximal pyroclastic deposits accumulated on the flanks of the SEC during the explosive eruptive activity (Behncke, 2009; Norini et al., 2009; Andronico et al., 2018), although other mechanisms have been also suggested for past events, such as phreatomagmatic explosions resulting from interaction between magma and hydrothermally altered rock/snow or rapid decompression of gas-rich magma induced by the flank sliding of the SEC during the November 16, 2006 event (Behncke et al., 2008; Ferlito et al., 2010).

To date, a hazard map associated with pyroclastic avalanche inundation at the summit of Mt. Etna is lacking. A hazard map can be developed by combining probabilistic analysis with the deterministic numerical modeling of the flow propagation, which is a valuable tool to predict the most likely paths of the avalanches over the topography. Here, to simulate the propagation of pyroclastic avalanches, we adopted the shallow water numerical code IMEX-SfloW2D, which is based on the continuum approach to model granular flows, for which the thickness is small compared to their characteristic lengths. Given the low computational costs, depth-averaged balance equations of the mass and momentum are commonly adopted to simulate the emplacement of granular flows, represented as a gas-particle mixture, coupled with a rheological model for the frictional forces (Pudasaini and Hutter, 2007; de' Michieli Vitturi et al., 2019). The complex and still poorly understood rheology of the polydisperse granular mixture associated with pyroclastic avalanches poses several difficulties in simulating their propagation and emplacement. In this regard, the Voellmy-Salm rheology model, commonly used for avalanches and debris flows, has been considered to be suitable for volcanic gravitational flows. This model considers the gas-particle mixture as a homogeneous mass and whose motion is controlled by two parameters: the dry-friction coefficient μ and the viscous-turbulent friction coefficient ξ. However, for pyroclastic avalanches there are no direct measurements of these parameters, so their values cannot be easily defined a priori. An attempt to calibrate the values of μ and ξ through a semi-empirical approach was reported by de' Michieli Vitturi et al. (2019), who used the open-source code IMEX-SfloW2D to reproduce the pyroclastic avalanche occurred at Mt. Etna volcano on February 11, 2014 (Andronico et al., 2018) by varying the rheological parameters in a range consistent with previous studies of other geophysical granular avalanches (Bartelt et al., 1999).

In this study, we present an automated workflow developed to run an ensemble simulations based on a Monte Carlo approach with the aim to: i) explore the sensitivity of the simulated pyroclastic avalanches on the unknown parameters and to perform a calibration of the rheological parameters; ii) generate probabilistic maps for the invasion of avalanches, considering the variability of the unknown parameters.

The well-documented pyroclastic avalanches occurred during the February 10, 2022 paroxysmal eruption at Mt. Etna volcano was used as a case study. The method presented here allowed us to investigate the effects of modification in the topography on flow propagation and its emplacement and to define ranges of uncertainties for the unknown rheological parameters. Finally, based on the result of the calibration of the input parameters, we developed a probabilistic hazard map associated with a potential scenario on the summit area of Mt. Etna, by considering the whole SEC as a source area in order to draw the more likely areas that can be affected by the pyroclastic avalanche propagation.

2. Pyroclastic avalanches at Mt. Etna and the 10 February 2022 episode

Emplacement of pyroclastic avalanches on Mt. Etna has become more frequent in the last 20 years. Most of them were generated at the SEC, the most active of the summit craters, which at the time of the case study/studied lava fountain was around 3347 m high (Ganci et al., 2022). The increase of the explosive summit activity led to the formation of a composite scoria cone, which has been characterized by a rapid growth due to the accumulation of pyroclastic materials during the 2000-2001 and the 2011-2013 eruptive sequences (Behncke et al., 2006; 2014; De Beni et al., 2015). The construction phases have been alternated with destructive phases when the mechanical conditions reach the instability, leading to partial collapses of the scoria cone and then the formation of pyroclastic avalanches. The most notable avalanches have been observed during the November 16, 2006 eruption and on February 11, 2014 (Norini et al., 2009; Behncke, 2009; Andronico et al., 2018). However, starting from 13-14 December 2020, which marked the beginning of the powerful 2020-2022 paroxysmal series (Andronico et al., 2021; Corsaro and Miraglia, 2022; Giuffrida et al., 2023), a further increase in frequency of pyroclastic avalanches characterized the volcanic activity at summit (De Beni et al., 2024; Zuccarello et al., submitted).

During the powerful lava fountaining episode that occurred on February 10, 2022 a large pyroclastic avalanche was observed (Fig. 1). The prelude of the eruption started with the resumption of the Strombolian activity at the SEC in the night between February 9 and 10 after almost two months of quiescence. The Strombolian activity increased

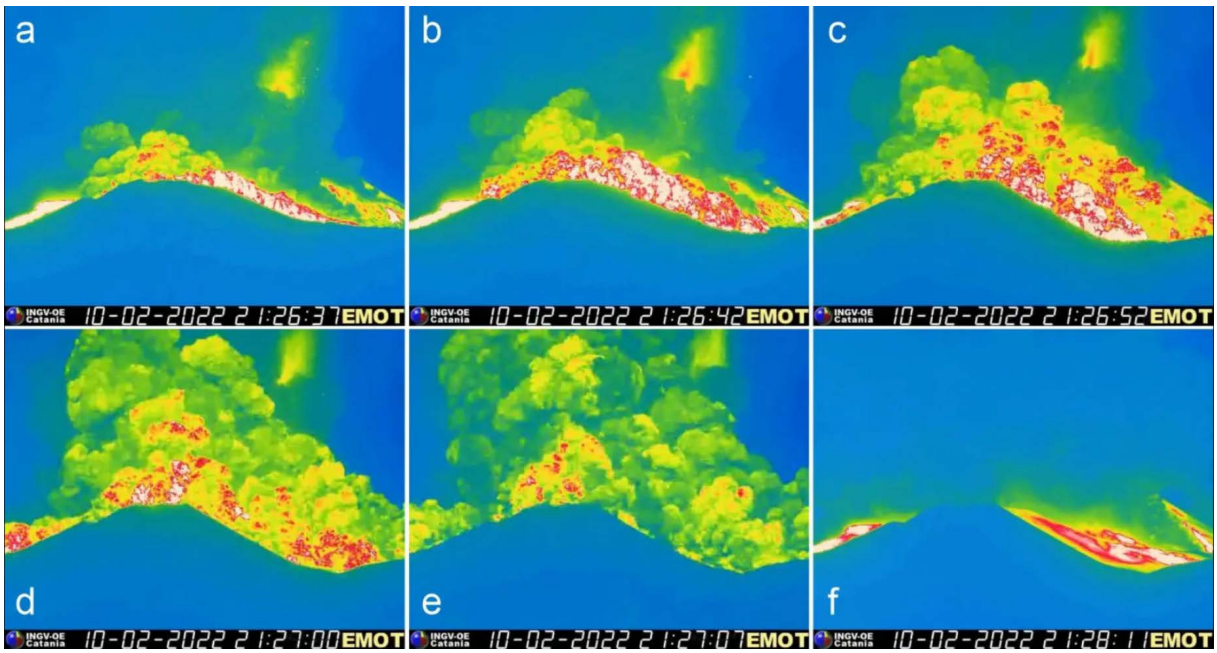

Figure 1. Frames captured by EMOT thermal camera of the INGV network showing the evolution of the pyroclastic avalanche occurred during the February 10, 2022 paroxysmal eruption at Mt. Etna (INGV-OEb, 2022b).

during February 10, accompanied by lava effusion at south-southwest of the SEC, and culminating in the evening of the same day with a spectacular lava fountaining above 1000 m and formation of a pyroclastic-column high ~12 km a.s.l. (INGV-OE, 2022b). During the peak of the lava fountaining, some pyroclastic avalanches were emplaced on the south and east flank of the SEC. The main avalanche was generated at 21:26 UTC from the south flank of the SEC where an effusive vent was feeding a lava flow before the collapse. The pyroclastic avalanche propagated southward for a duration of ~60-80 s, reaching an altitude of 2750 m a.s.l., covering the upper scoria cone of the 2002-2003 eruption, where there is a path for hikers, and partially burning a small wooden shelter of the Civil Protection of the Sicilian Region that was located at 2798 m a.s.l. at the eastern base of the cone (Fig. 2).

A huge detachment scar on the south flank of the SEC was visible after the emplacement of the pyroclastic avalanche, from where a new lava flow was emitted until the end of the eruption. The reddish-brown deposit of the

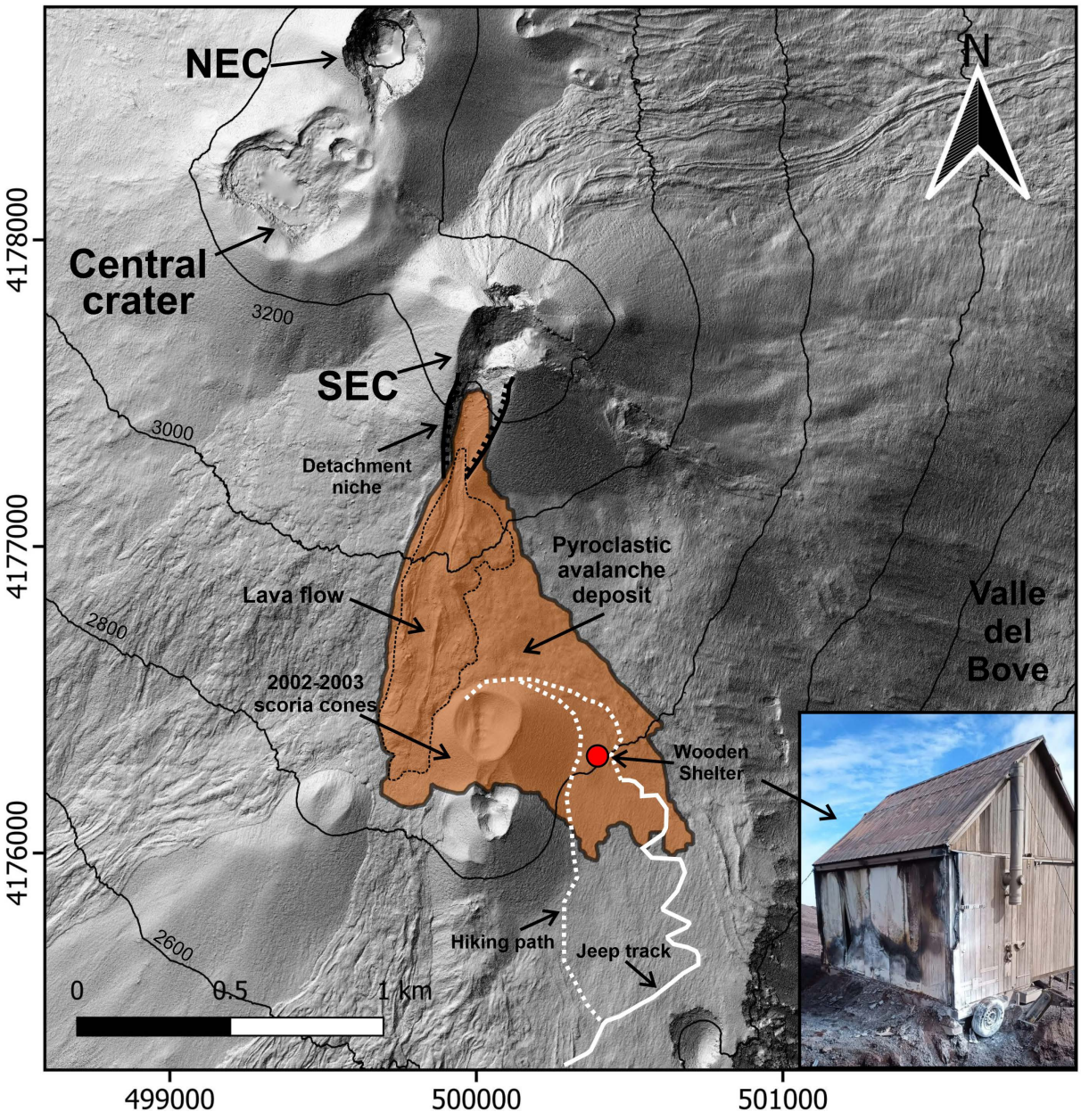

Figure 2. Map of the Mt. Etna summit with the main active craters (SEC: South East Crater; NEC: North East Crater; BN: Bocca Nuova; VOR: Voragine). The brown area is the deposit of the main pyroclastic avalanche emplaced during the February 10, 2022 eruption. The red spot indicates the location of the wooden shelter shown in the inset figure. The solid white line indicates the path used by the jeeps, the dashed white line is the hiking path used by the tourists and hikers. The background image is the shaded relief of a satellite-derived Digital Surface Model updated to June 2022 (Ganci et al., 2023). Photo by Francesco Ciancitto.

main pyroclastic avalanche is composed of fine ash-lapilli to decametric blocks and shows a fan shape, extending up to 1.4 km from the base of the scar towards the upper scoria cone of the 2002-2003 eruption and covering an area of ~0.70 km^2 (Fig. 2). The deposit thickness along the east lobe ranges from 0.05 m to ~0.65-0.70 m and is greater than 1 m. In some areas on the portion between the 2002-2003 cones and the SEC, the deposit is covered by lava flows emitted after the emplacement of the pyroclastic avalanche, preventing direct observation of the stratigraphic sections (Zuccarello et al., submitted).

3. The open-source code IMEX-SfloW2D

With respect to the original model adopted for the simulation of pyroclastic avalanches and presented in de' Michieli Vitturi et al. (2019), here we use an improved version of the open-source code IMEX-SfloW2D (de' Michieli Vitturi et al., 2023). The model equations are written in Cartesian coordinates over a topography that does not change with time. The two velocities u(x, y, t) and v(x, y, t) (averaged over the vertical flow thickness h) are defined as the components along the x and y axes orthogonal to the z axis, parallel to the gravitational acceleration.

If we denote with ρm the density of the gas-particle mixture, conservation of mass for the flow is written as:

$$\partial \rho mh/\partial t + \partial(\rho mhu)/\partial x + \partial(\rho mhv)/\partial y = 0 \quad (1)$$

For this application, with respect to the full model presented in de' Michieli Vitturi et al. (2019; 2023), no erosion and deposition are considered, as well as air entrainment.

Assuming a hydrostatic pressure distribution along the vertical component, and introducing the notation g′ for the reduced gravity $g' = [(\rho m - \rho a)/\rho m]g$, where ρa is the atmospheric density, the equations for the momentum components are:

$$\partial(\rho mhu)/\partial t + \partial/\partial x[\rho mhu^2 + \rho mg'(h^2/2)] + \partial/\partial y(\rho mhuv) = -\rho mg'h\,\partial B/\partial x + F_x \quad (2)$$

$$\partial(\rho mhv)/\partial t + \partial/\partial x(\rho mhuv) + \partial/\partial y[\rho mhv^2 + \rho mg'(h^2/2)] = -\rho mg'h\,\partial B/\partial y + F_y \quad (3)$$

where B is the topography elevation and F_x and F_y are the two components of the friction force F. For the application presented in this work, the Voellmy-Salm rheology is used, which split the total basal friction in two components: (1) a velocity-independent term proportional to the dry-friction coefficient μ; and (2) a velocity-dependent term inversely proportional to the viscous-turbulent friction coefficient ξ and commonly considered representing the effect of granular collisions:

$$F = (F_x, F_y) = -(u, v)/(u^2 + v^2)^{1/2}\,\rho m[\mu\, hg' \cdot n + g/\xi\,(u^2 + v^2)] \quad (4)$$

Finally, if we denote with C_v the mass averaged specific heat of the gas-particles mixture and with T its temperature, a transport equation for the specific thermal energy C_v T is solved:

$$\partial/\partial t(\rho m\, hC_vT) + \partial/\partial x(C_vT\,\rho m\, hu) + \partial/\partial y(C_vT\,\rho m\, hv) = 0 \quad (5)$$

The model requires different input parameters, including the total duration of the simulation, a Digital Surface Model (DSM) of the topography defining the terrain elevation B(x, y), the computational domain extent for the simulation of the flow propagation, the volume and the location of the material involved, the physical parameters of

solid and gas fraction, and the rheological parameters of the friction model. The simulations are run on a uniform grid of equally sized square pixels, by adopting a finite-volume central-upwind scheme in space, and an implicit-explicit Runge-Kutta scheme (IMEX) for the discretization in time (Pareschi and Russo, 2005).

4. The workflow development

A series of Python scripts have been developed to automate the full workflow (from the pre-processing to the post-processing), allowing to perform the statistical calibration of input parameters and to produce hazard maps (Fig. 3). Pre-processing scripts generate an ensemble of n samples (up to 10^4 scenarios), whereas post-processing scripts perform the fit between the area covered by the simulated and the real avalanches and/or combine the output files derived from all simulations to generate the probabilistic maps. The ensembles of simulations have been performed on the parallel cluster at Istituto Nazionale di Geofisica e Vulcanologia (INGV) – Sezione di Pisa. For this study, the computational time required for each simulation is of a few minutes on a single core.

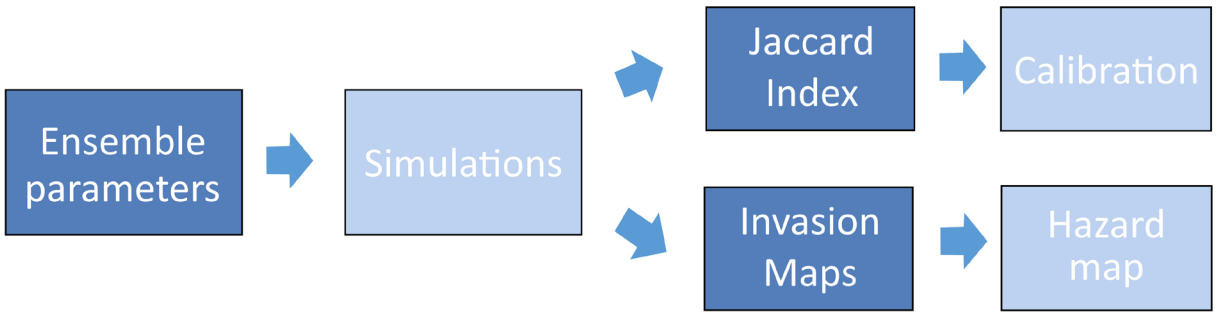

Figure 3. Flowchart of the workflow

The input parameters defined in the pre-processing are the location and geometry of the source of the avalanche, the involved volume, the rheological parameters μ and ξ, and the initial velocity u_0 of the avalanche. Each parameter has been sampled considering a specific distribution (e.g., normal, triangular, uniform) within a defined range. The initial conditions are defined by excavating a volume on the topography with an ellipsoidal shape oriented to the local maximum slope. The source location is given as x and y coordinates of the highest point of the detaching volume, and the ellipsoid axes are computed by the preprocessing script with an iterative procedure to obtain the desired volume extracted from the intersection between the topography and the excavated ellipsoid (defined as a prolate spheroid with an aspect ratio of 3.0 between the largest and smaller axis; Fig. 4a). A new DSM reporting the excavated substrate is then created for each simulation, while the initial avalanche volume is obtained by the difference between the original and the modified topography (Fig. 4b).

The IMEX-SfloW2D code is run to simulate the pyroclastic avalanche emplacement for each combination of the input parameters defined in the ensemble. Every simulation is performed within a defined domain area and several outputs are saved as ESRI ASCII files. These output files include the flow thickness at defined times, the maximum (over time) thickness of the flows in each cell of the DSM, and a series of binary maps for the simultaneous exceedance, within the timespan of the simulation, of combinations of prescribed thickness and dynamic pressure threshold values (6 threshold values for the thickness and 5 for the dynamic pressures, for a total of 30 combinations).

For the calibration of the velocity and the rheological input parameters, the Jaccard Index (J; Aravena et al., 2022) has been used to evaluate the fit between each simulated avalanche and the observed deposit emplaced during the February 10, 2022 eruption, calculated as the ratio between the intersection and the union of the simulated (A) and real (B) areas:

$$J(\mathrm{A},\mathrm{B}) = \mathrm{A} \cap \mathrm{B} / \mathrm{A} \cup \mathrm{B} \tag{6}$$

Then, a threshold was defined to choose the simulations that better reproduce the observed invaded area. Here, we have selected $J = 0.60$ as threshold value.

Finally, a new ensemble of simulations is defined on the base of the results of the calibration. In particular, the combinations of the input parameters associated to the best simulations with $J > 0.60$ have been sampled with equal probabilities as input to run a new ensemble in order to build the probabilistic map, including also variations in the volume and the initial position of mobilized material. In this regard, the post-processing phase consists of integrating the areas affected by all simulated pyroclastic avalanches from the second ensemble to draw the probabilistic hazard map. The probability of the invasion in each pixel of the grid has been estimated as the fraction of the considered simulations for which the pixel was invaded by the flow. Different maps can also be created as a function of the volume of simulated avalanches, by estimating the probability conditioned on the occurrence of a pyroclastic avalanche within the considered volume class. These maps represent the probability of inundation associated with a single event and the exposition time is not included in the computation.

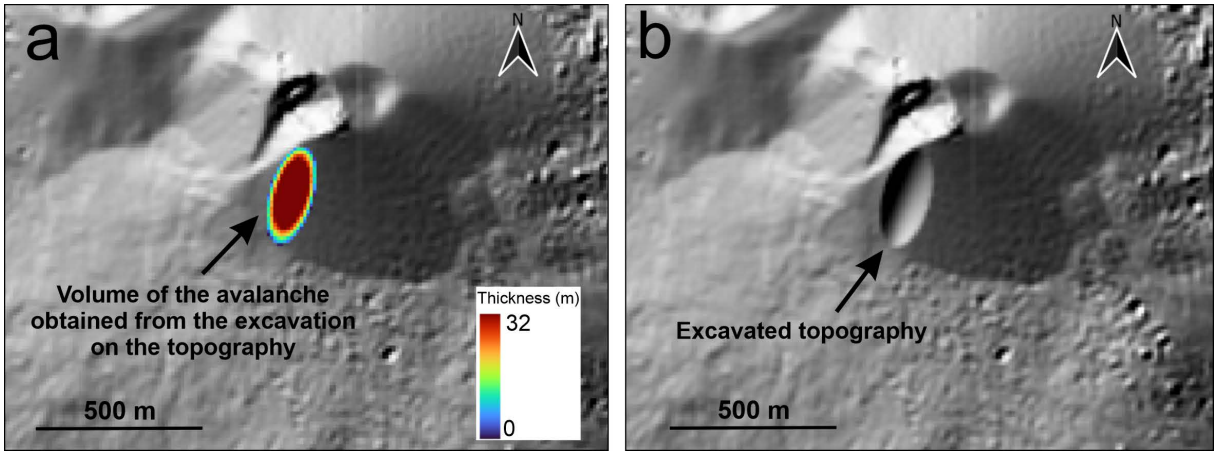

Figure 4. (a) Geometry of the excavated volume used to run the pyroclastic avalanche simulation on the pre-eruptive DSM derived by satellite images acquired in July 2021 (Ganci et al., 2023); (b) the new DSM reporting the excavated substrate used for the simulation.

5. Setting of the parameters for the workflow

5.1 Calibration of the rheological parameters and initial velocity

An ensemble of N = 300 simulations has been defined for the calibration of the unknown input parameters to reproduce the February 10, 2022 pyroclastic avalanche. The July 2021 DSM of the Mt. Etna summit (Ganci et al., 2023) has been used as topography over which the simulations have been performed. In Ganci et al. (2023), the difference between the pre- and post-eruptive DSM (July 2021 and June 2022, respectively) provided the variation of the thickness in the detachment area before and after the collapse, allowing to estimate the volume of the material involved during the collapse of 1.61×10^6 m$^3 \pm 0.1$. However, assuming that a fraction (approx. 35%, Sparks and Walker, 1977) of this volume has been dispersed in the ash-cloud through elutriation of the thinnest particles (not modeled in the simulation), for all the calibration simulations of the pyroclastic avalanche we considered an initial volume of $V = 1.0 \times 10^6$ m^3. This volume has been used for a unique source located on the south flank of the SEC, obtained by excavating the digital topography with an ellipsoidal shape (Fig. 4).

The rheological parameters μ and ξ have been sampled randomly within defined ranges considering uniform distributions, respectively of 0.20-0.55 and 300–900 m/s^2. We included also the initial velocity u_0 of the mobilized material as input parameter for the calibration, with discrete values sampled within the range 0-140 m/s at steps of 20 m/s assuming a uniform distribution (i.e. 0 m/s, 20 m/s, 40 m/s, … 140 m/s). The total time of each simulation of the ensemble has been fixed at 240 s. From all the 300 combinations of rheological parameters and initial velocity values, we selected only those producing a J greater than 0.60 for the comparison of the area invaded with that of the 10 February 2022 pyroclastic avalanche.

5.2 Development of the hazard map

The combinations selected from the calibration have been used to generate a new ensemble of 3000 simulations to construct the hazard map. For the new ensemble, we used the DSM representing the topography of the summit in June 2022 (Ganci et al., 2023), with the entire SEC as the potential source of the pyroclastic avalanche. The coordinates of the highest point of the detaching volume were sampled randomly considering a uniform spatial distribution (Fig. 5). The lower part of the crater has not been sampled in order to prevent the excavation of the volume that would interest the flat area around the SEC. We also sampled the volume in the range of 0.5 – 3.0 × 10^6 m^3 considering discrete values with variations of 0.5 × 10^6 m^3. In this regard, the volumes were sampled with different weights. Since a quantitative record of pyroclastic avalanche volumes at Mt. Etna is missing, we choose to assign the weights using data from literature. Brunetti et al. (2009) proposed a law for the probability distribution of occurrence of a landslide as a function of the volume of material involved, by integrating quantitative data of different types of landslides that occurred in various environments (e.g. sub-aerial, submarine). In particular, we used the power law (Eq. (1) in Brunetti et al., 2009) to obtain the cumulative number of landslides as a function of the volume. We calculated the cumulative number for intervals of 0.5 × 10^6 m^3, choosing the upper bound of each interval as representative.

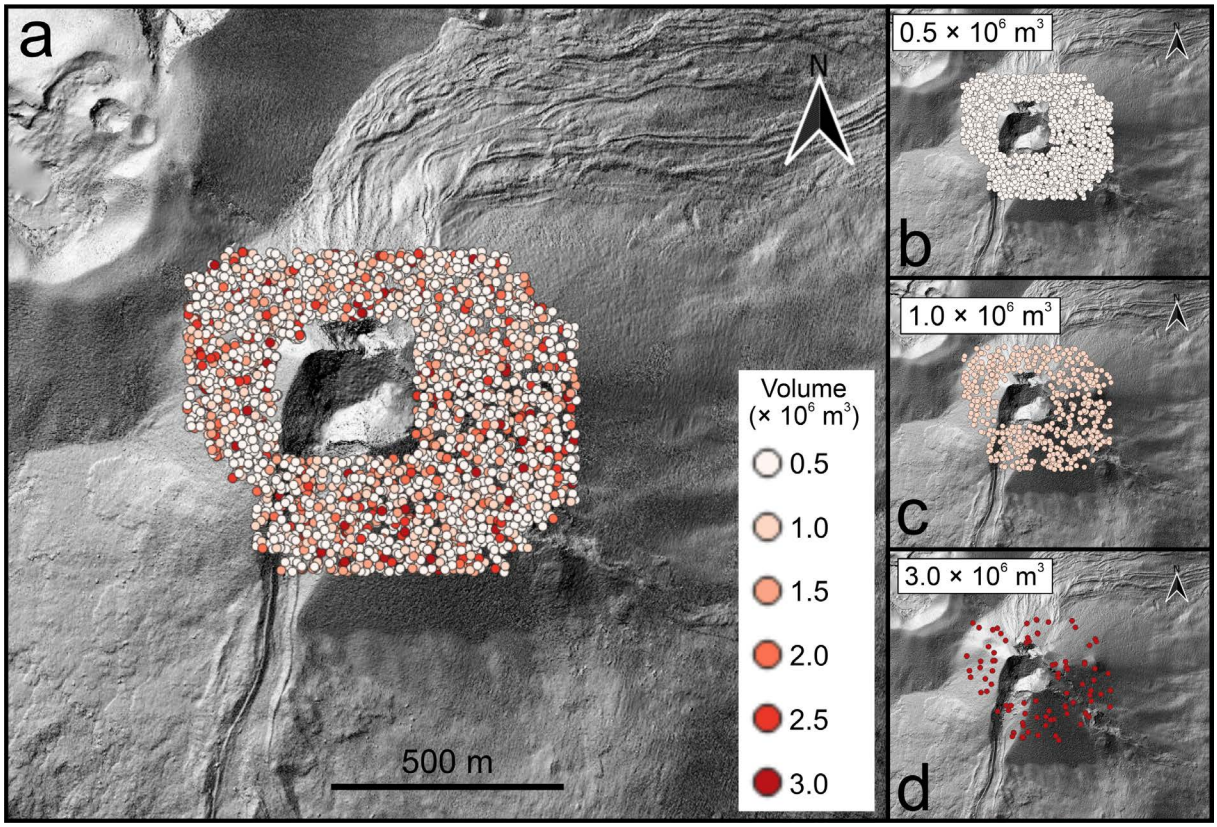

Figure 5. Locations of the 3000 sources on the June 2022 DSM for the development of the hazard map (a). Selected sources for defined volume are shown in the panel for volumes of 0.5 × 10^6 m^3 (b), 1.0 × 10^6 m^3 (c), and 3.0 × 10^6 m^3 (d). The dots reported in the map represent the coordinates of the highest points of the detaching volumes that have been excavated along to the local maximum slope.

6. Results

The simulated pyroclastic avalanches derived from the first ensemble, based on the random combinations of the input parameters, are characterized by very different invasion areas. In particular, the initial velocity strongly affects the emplacement of the simulated avalanches. When the velocity is set to zero, the simulated deposits are

more widespread and, at low μ, there are portions of the avalanche which propagated toward the Valle del Bove, located eastward the summit craters (Fig. 6a). For fixed values of the rheological parameters, the affected area by the simulated avalanches is progressively more confined as u_0 increases (Fig. 6b-d). Good fits between the observed and modeled avalanches are obtained for simulations characterized by velocities greater than 60 m/s.

For the calibration, a selection of the best-fit models has been made considering those models which provided the $J > 0.60$ (Table 1). The range of the best-fit values of μ, ξ and u_0 are respectively 0.22-0.52, 340-890 m/s^2, and 60-140 m/s, and the values of the simulation with the highest J (~0.69) are $\mu = 0.33$, $\xi = 741$ m/s^2 and $u_0 = 80$ m/s. However, simulations with μ values lower than 0.29 show that the avalanche motions stop at times greater than 200 s, while the observed avalanche has been emplaced in a time of <100 s. So, we do not consider as best fit values simulations with μ lower than 0.29. The simulated avalanches with $J > 0.60$ are characterized by thickness distributions slightly higher compared with field measurements, where available (Zuccarello et al., submitted). Figure 7 reports the correlation between the parameters, showing positive correlation between μ and ξ, μ and u_0 and negative for ξ and u_0.

The second ensemble of 3000 simulated pyroclastic avalanches generated considering the whole SEC as source were used to develop the probabilistic hazard maps. The total map obtained by combining all the simulations, and thus for the 0.5-3.0 × 10^6 m^3 volume interval, shows that the highest probability of inundation, estimated at 0.26, is localized at south-east of the SEC (Fig. 8). Relatively high probabilities are also observed in the east, north-east and south-west directions. The maximum computed runout is ~3.5 km, higher than the distance covered by the February 10, 2022 avalanche (although not reaching the cable car arrival at 2500 m a.s.l.), and the most distal areas (minimum > 1300 m from the source) are characterized by very low probabilities (<0.03). Figure 9 shows the hazard maps based on fixed volumes of simulated avalanches, and we can observe that the invaded area slightly varies being, as expected, more widespread as the volume increases. The figure also shows that probabilities become higher with increasing volumes, with a maximum probability of 0.23 for 0.5 × 10^6 m^3 and 0.38 for 3.0 × 10^6 m^3. We finally observe that, as shown in Fig. 5, the number of samples (i.e. the number of simulations) used to compute the probabilities is smaller for larger volumes (88 samples for 3.0 × 10^6 m^3), and this results in a less accurate statistical result compared to smaller volumes (1811 samples for 0.5 × 10^6 m^3).

μ	ξ (m/s^2)	u_0 (m/s)	J
0.45	708	120	0.6277
0.35	543	120	0.623
0.42	407	140	0.619
0.34	709	100	0.630
0.36	325	140	0.633
0.42	832	100	0.678
0.53	894	100	0.659
0.38	803	80	0.674
0.42	620	100	0.666
0.33	387	120	0.673
0.31	377	100	0.643
0.32	463	120	0.653
0.47	851	100	0.676
0.49	477	140	0.605
0.46	410	140	0.609
0.47	595	100	0.610
0.32	737	80	0.686

μ	ξ (m/s^2)	u_0 (m/s)	J
0.31	754	60	0.606
0.29	365	120	0.689
0.35	440	120	0.673
0.33	741	80	0.691
0.34	461	120	0.665
0.29	362	140	0.637
0.34	598	100	0.685
0.46	413	140	0.609
0.40	802	80	0.663
0.39	744	80	0.651
0.29	714	60	0.636
0.53	870	100	0.653
0.46	598	120	0.649
0.29	554	80	0.689
0.43	402	120	0.617
0.48	785	120	0.621
0.31	405	140	0.609
0.50	535	140	0.602
0.38	692	80	0.638
0.33	345	140	0.659
0.38	674	100	0.683
0.37	519	100	0.672
0.43	578	120	0.656
0.29	740	60	0.642
0.40	348	140	0.619
0.41	758	80	0.628
0.32	562	80	0.662
0.40	566	100	0.668
0.49	841	120	0.616
0.30	381	100	0.657
0.32	519	80	0.632
0.45	763	120	0.609
0.38	490	100	0.658
0.35	548	100	0.684

Table 1. Selected combination of rheological parameters and initial velocity which produced simulated avalanches with $J > 0.60$. The grey row highlights the best fit.

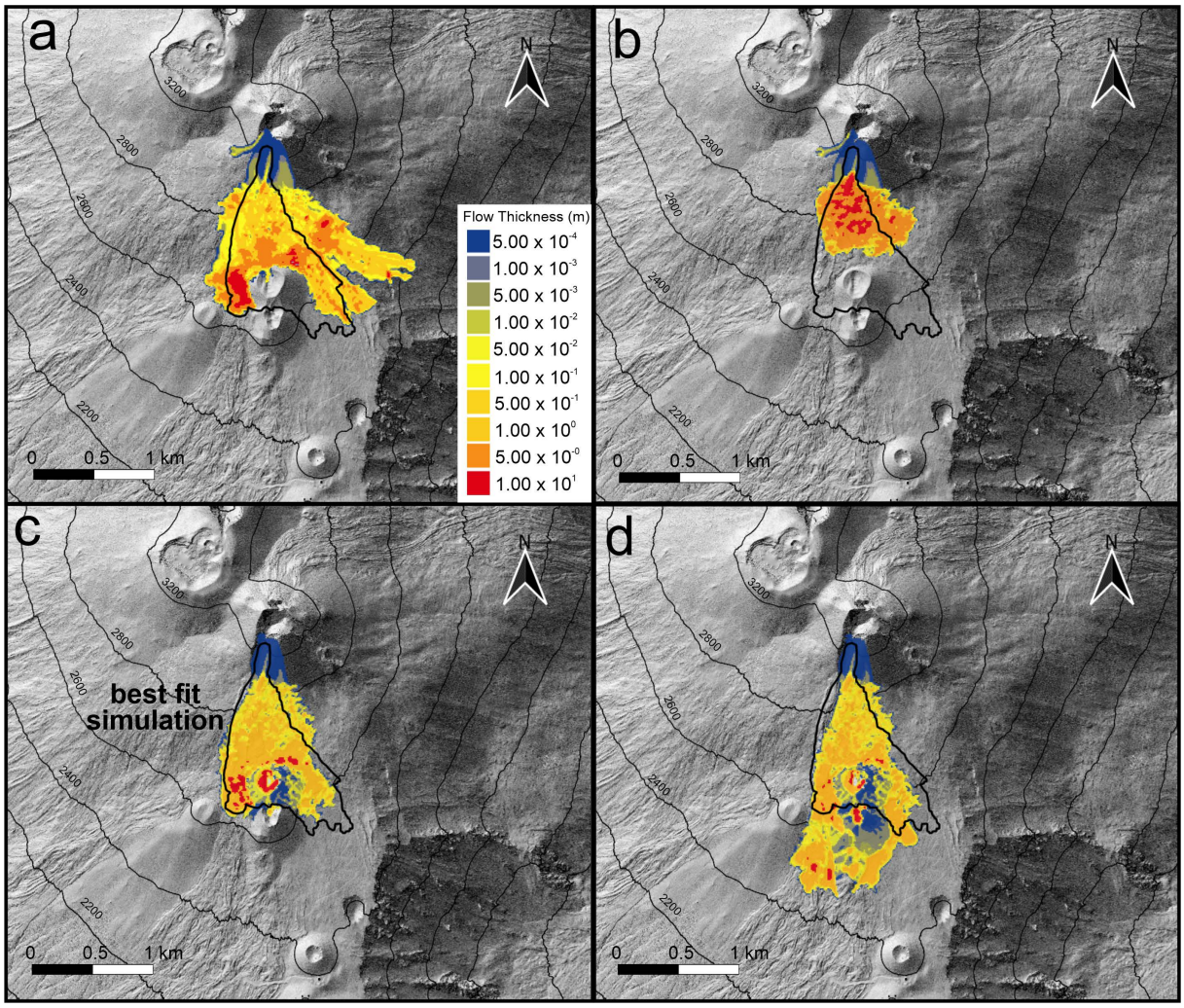

Figure 6. Runout of 4 simulations with different input values, using: (a) $\mu = 0.20$, $\xi = 300$ m/s^2, $u_0 = 0$ m/s, with $J = 0.375$; (b) $\mu = 0.33$, $\xi = 741$ m/s^2, $u_0 = 0$ m/s, with $J = 0.271$; (c) $\mu = 0.33$, $\xi = 741$ m/s^2, $u_0 = 80$ m/s, with $J = 0.691$(best fit simulation); (d) $\mu = 0.33$, $\xi = 741$ m/s^2, $u_0 = 140$ m/s, with $J = 0.467$. The black line marks the area covered by the February 10, 2022 deposit.

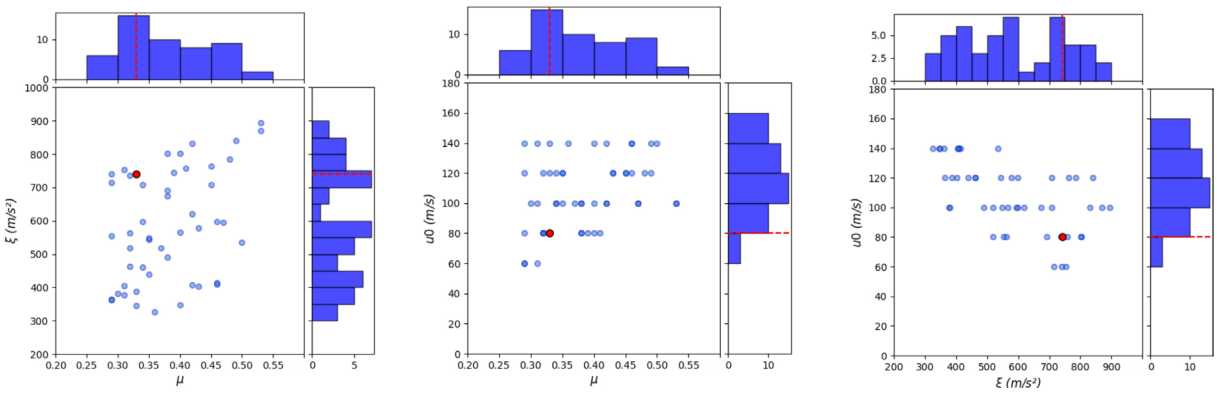

Figure 7. Scatter plots and histograms of the input parameters investigated for the calibration. The red lines and red dots are associated with the best fit values.

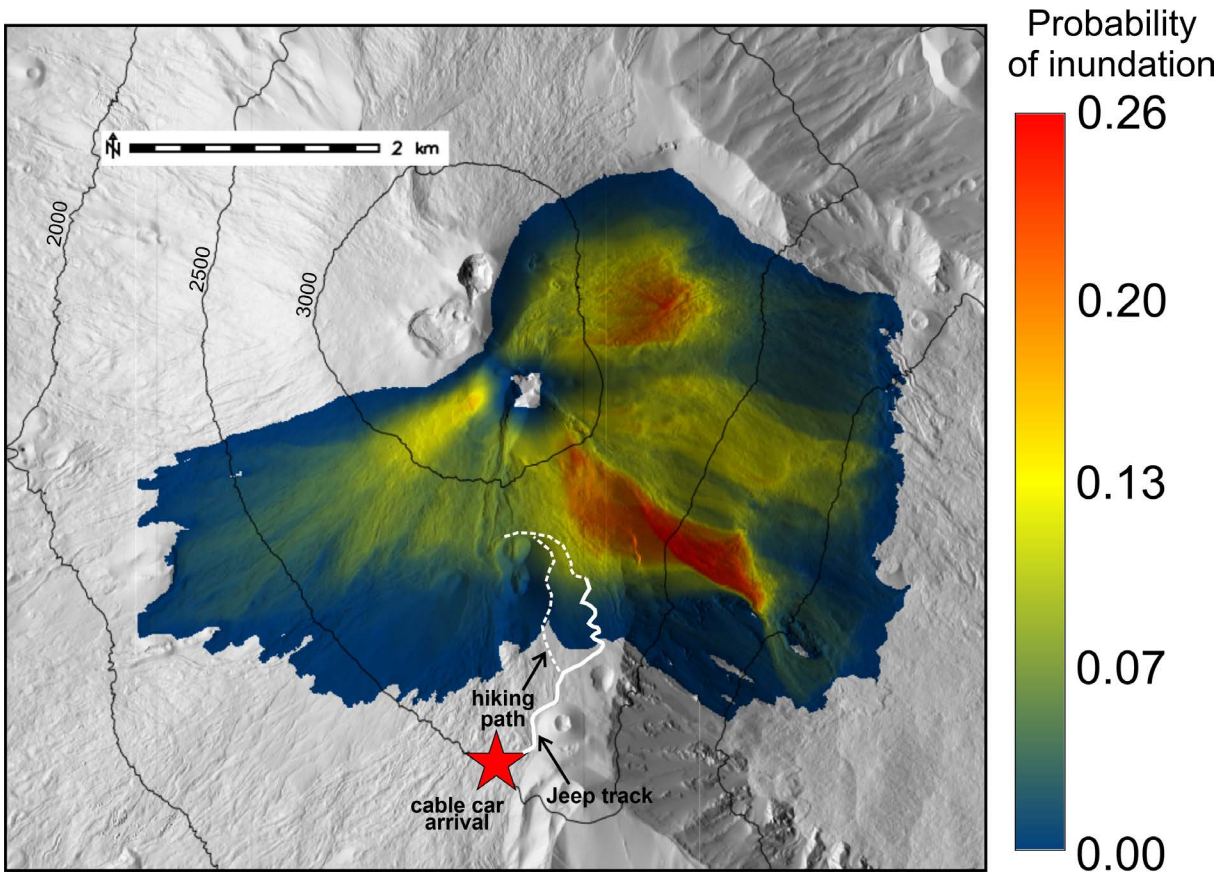

Figure 8. Probabilistic hazard map linked to pyroclastic avalanche inundation considering all the 3000 runs of the ensemble, with volumes from 0.5 to 3.0 × 10^6 m^3 and using the combinations of the input parameters obtained from the calibration. The probabilities have been estimated by computing the times that each point has been invaded by simulated flows over the total number of simulations. The dashed white line is the hiking path, the solid line the jeep track and the red star indicates the location of the cable car arrival at 2500 m a.s.l.

7. Discussion and conclusions

The results of the calibration are primarily dependent by the choice of the input parameters and the range within which they are investigated. The range explored for the rheological parameters, which is one of the targets of the calibration, is consistent with values used in previous studies and for other granular flows (Bartelt et al., 1999; de' Micheli Vitturi et al., 2019). As regards the initial velocity, by comparing the results of the simulations with the observations, we noticed that an initial momentum is required to properly reproduce the observed pyroclastic avalanche that occurred on February 10, 2022. In particular, a high kinetic energy is necessary to obtain good fit values with the observed distribution of the deposit, with velocity greater than 60 m/s. Indeed, at lower velocities simulated avalanches show a wider spread out covering areas that were not affected by the actual avalanche. Moreover, the simulated avalanches with low initial velocities, but with rheological parameters values similar to those of the best fit ($\mu = 0.33$, $\xi = 741$ m/s^2), were not able to overcome the upper scoria cone of the 2002-2003 eruption as observed in the field, where thicknesses up to ~80 cm have been measured on the border of the crater (Zuccarello et al., submitted). This feature has been reproduced in the simulations by providing high initial velocities to the mobilized volcanic material. Therefore, an additional mechanism to the slope instability must be invoked. The movement of the magma body toward the active vent on the SEC flank, which was feeding the effusive activity before the collapse, has induced the instability of the cone, with a dynamic similar to that described in Andronico et al. (2018) for the February 11, 2014 avalanche. We hypothesize that the decompression induced by the collapse of the cone may have led to the expansion of the fluid phase released by the pushing magma potentially associated with an explosive process or, alternatively, with the unloading and expansion of the overheated

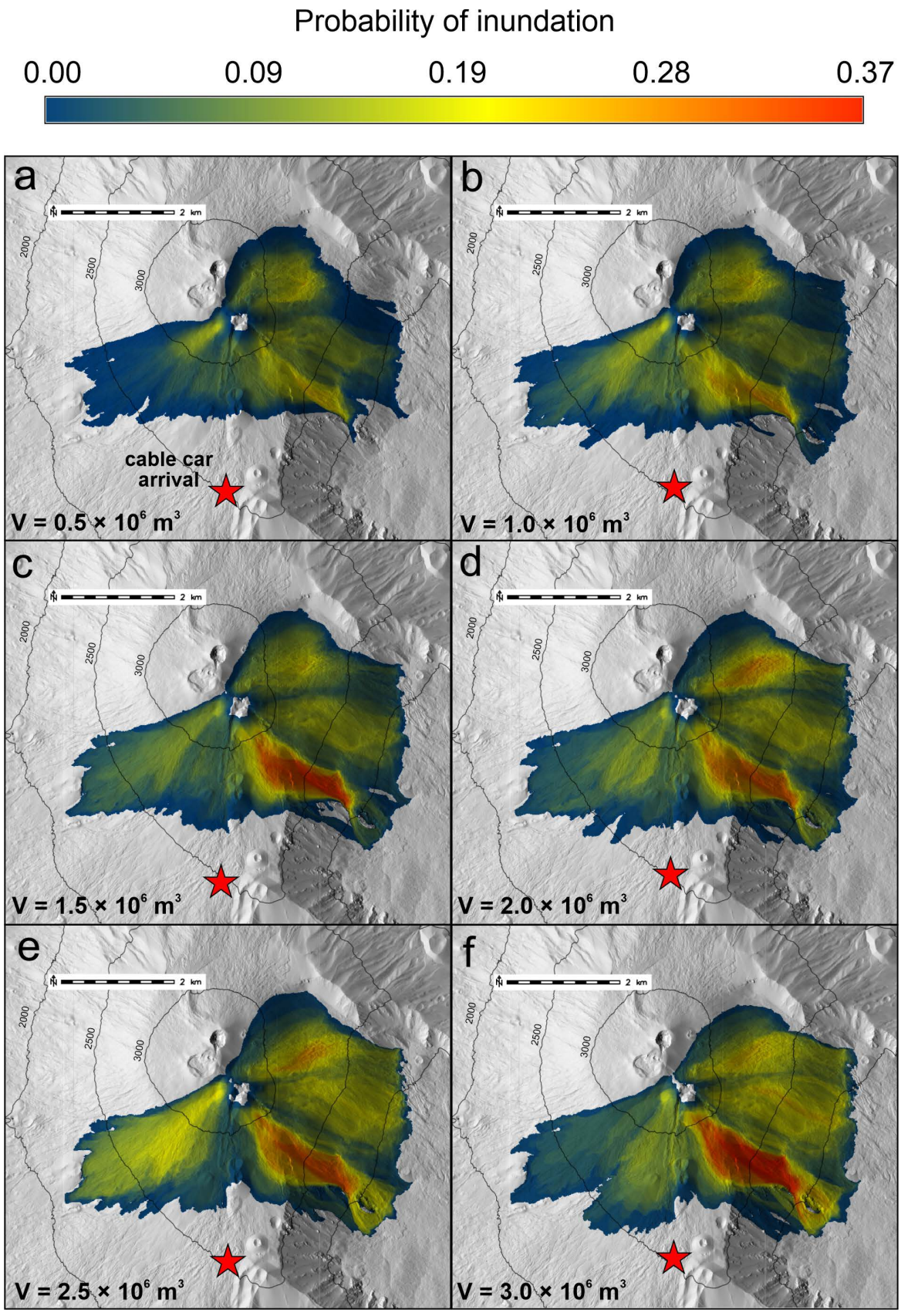

Figure 9. Probabilistic hazard maps linked to the pyroclastic avalanche inundation hazard maps considering simulations associated to volumes of: (a) 0.5×10^6 m^3; (b) 1.0×10^6 m^3; (c) 1.5×10^6 m^3; (d) 2.0×10^6 m^3; (e) 2.5×10^6 m^3; (f) 3.0×10^6 m^3. Please note that the probability intervals for each panel are different and are conditioned on the occurrence of a pyroclastic avalanche within a specific volume class. The red star indicates the location of the cable car arrival at 2500 m a.s.l.

hydrothermal fluids trapped within the cone, contributing to provide the high initial kinetic energy of the mobilized material assumed for the initial conditions to model the avalanche propagation (Zuccarello et al., submitted). From another hand, for our simulations we assumed constant values of the rheological parameters during the propagation of the flow, while we cannot rule out that complex dynamics may affect the rheological behavior of the pyroclastic avalanches. Processes such as the buildup of pore pressure or self-fluidization can take into account such variations in the rheological parameters (e.g. Roche, 2012, Gueugneau et al., 2017; Lube et al., 2019; Breard et al., 2019). As well as substrate erosion and/or depositional mechanisms may control variations in the rheology (Brand et al., 2014; Sulpizio and Dellino 2008). However, further studies with different rheological models or non-constant values of the rheological parameters are required to better investigate the dynamics of pyroclastic avalanche propagation.

Based on the results of the calibration, the second ensemble of simulations of pyroclastic avalanches allowed us to draw the areas more likely affected by the propagation of future avalanches, considering an updated DSM of Mt. Etna and the whole SEC as possible source. The variability of the affected area has been investigated also as a function of the volume of the mobilized material. Despite the occurrence of pyroclastic avalanches with volumes greater than 1.0×10^6 m^3 have not yet been observed, the choice to sample volumes up to 3.0×10^6 m^3 is justified because we cannot exclude that larger volumes may be involved in future pyroclastic avalanches, due to the current morpho-structural setting of the SEC which could potentially undergo further collapses (Zuccarello et al., submitted). The more likely invaded areas outlined by the hazard map are consistent with the observation of recent pyroclastic avalanches generated during the 2020-2022 paroxysmal sequences. Though the arrival point of the cable car at 2500 m is not inundated by any simulated avalanches, the area with the highest probability of inundation is located at south-east of the SEC, still being one of the most frequented area by tourists and must be taken into consideration for the risk management related to summit activity for future eruptions. It is noteworthy that a continuously updated digital model of the ground surface is necessary in volcanoes like Etna, where the frequent eruptive activity can deeply modify not only the morphology but also the roughness of the summit area, thus influencing the path of future pyroclastic avalanches. At the time of writing, for example, the intense paroxysmal activity at the VOR has completely buried both the PDC and the lava and tephra deposits accumulated at the foot of the SEC after February 10, 2022.

The workflow specifically developed for this application is a useful tool to run an ensemble characterized by a high number of numerical simulations and to perform the calibration of unknown input parameters and to derive hazard maps. The ability to utilize an HPC-based technology for the workflow enables us to run a large number of simulations in a very short time (from minutes to a few hours) and quickly produce hazard maps. This is crucial for managing volcanic crises, as morphological changes caused by collapses and pyroclastic avalanches require updates of the maps after each event to guarantee accurate predictions of the most likely paths that could be affected by the propagation of pyroclastic avalanches.

This work has represented a fundamental contribution for civil protection purposes. In fact, the hazard map produced has been used by the regional civil protection to re-delimit the access zone of the summit area of Etna as a safety measure.

Data availability statement. The code IMEX-SfloW2D is open source and can be freely downloaded at https://github.com/demichie/IMEX_SfloW2D_v2.

Acknowledgements. This work was supported by the INGV project Pianeta Dinamico (CUP D53J19000170001) funded by MIUR ("Fondo finalizzato al rilancio degli investimenti delle amministrazioni centrali dello Stato e allo sviluppo del Paese," legge 145/2018), Tema 8 – PANACEA 2021-2023.

References

Aravena, A., A. Bevilacqua, M. de' Michieli Vitturi, T. Esposti Ongaro et al. (2022). Calibration strategies of PDC kinetic energy models and their application to the construction of hazard maps, Bull. Volcanol., 84, 29, doi:10.1007/s00445-022-01538-8.

Andronico, D., A. Di Roberto, E. De Beni, B. Behncke et al. (2018). Pyroclastic density currents at Etna volcano, Italy: The 11 February 2014 case study, J. Volcanol. Geotherm. Res., 357, 92-105, doi:10.1016/j.jvolgeores.2018.04.012.

Andronico, D., A. Cannata, G. Di Grazia and F. Ferrari (2021). The 1986-2021 paroxysmal episodes at the summit craters of Mt. Etna: Insights into volcano dynamics and hazard, Earth Sci. Rev., 220, 103686, doi:10.1016/j.earscirev.2021.103686.

Bartelt, P., B. Salm and U. Gruber (1999). Calculating dense-snow avalanche runout using a Voellmy-fluid model with active/passive longitudinal straining, J. Glaciol., 45, 150, 242-254, doi:10.3189/s002214300000174x.

Behncke, B., M. Neri, E. Pecora and V. Zanon (2006). The exceptional activity and growth of the Southeast Crater, Mount Etna (Italy), between 1996 and 2001, Bull. Volcanol., 69, 149-173, doi:10.1007/s00445-006-0061-x.

Behncke, B., S. Calvari, S. Giammanco, M. Neri et al. (2008). Pyroclastic density currents resulting from the interaction of basaltic magma with hydrothermally altered rock: an example from the 2006 summit eruptions of Mount Etna, Italy, Bull. Volcanol., 70, 10, 1249-1268, doi:10.1007/s00445-008-0200-7.

Behncke, B. (2009). Hazards from pyroclastic density currents at Mt. Etna (Italy), J. Volcanol. Geotherm. Res., 180, 2-4, 148-160, doi:10.1016/j.jvolgeores.2008.09.021.

Behncke, B., S. Branca, R. A. Corsaro, E. De Beni et al. (2014). The 2011-2012 summit activity of Mount Etna: Birth, growth and products of the new SE crater, J. Volcanol. Geotherm. Res., 270, 10-21, doi:10.1016/j.jvolgeores.2013.11.012.

Brand, B. D., C. Mackaman-Lofland, N. M. Pollock, S. Bendaña et al. (2014). Dynamics of pyroclastic density currents; conditions that promote substrate erosion and self-channelization; mount St Helens, Washington (USA), J. Volcanol. Geotherm. Res., 276, 189-214, doi:10.1016/j.jvolgeores.2014.01.007.

Breard, E. C. P., J. R. Jones, L. Fullard, G. Lube et al. (2019). The Permeability of volcanic mixtures-Implications for pyroclastic currents, J. Geophys. Res. Solid Earth, 124, 1343-1360, doi:10.1029/2018JB016544.

Brunetti, M. T., F. Guzzetti and M. Rossi (2009). Probability distributions of landslide volumes, Nonlinear Process. Geophys., 16, 2, 179-188, doi:10.5194/npg-16-179-2009.

Calvari, S., F. Di Traglia, G. Ganci, F. Giudicepietro et al. (2020). Overflows and Pyroclastic Density Currents in March-April 2020 at Stromboli Volcano Detected by Remote Sensing and Seismic Monitoring Data, Remote Sens., 12, 3010, doi:10.3390/rs12183010.

Corsaro, R. A. and L. Miraglia (2022). Near real-time petrologic monitoring on volcanic glass to infer magmatic processes during the February-April 2021 paroxysms of the South-East Crater, Etna, Front. Earth Sci., 10-2022, doi:10.3389/feart.2022.828026.

Charbonnier, S. J., F. Garin, L. A. Rodríguez, K. Ayala et al. (2023). Unravelling the dynamics and hazards of the June 3rd, 2018, pyroclastic density currents at Fuego volcano (Guatemala), J. Volcanol. Geotherm. Res., 436, 107791, doi:10.1016/j.jvolgeores.2023.107791.

De Beni, E., B. Behncke, S. Branca, I. Nicolosi et al. (2015). The continuing story of Etna's New Southeast Crater (2012-2014): Evolution and volume calculations based on field surveys and aero-photogrammetry, J. Volcanol. Geotherm. Res., 303, 175-186, doi:10.1016/j.jvolgeores.2015.07.021.

De Beni, E., C. Proietti, S. Scollo, M. Cantarero et al. (2024). A hidden eruption: the 21 May 2023 paroxysm of the Etna Volcano (Italy), Remote Sens., 16, 1555, doi:10.3390/rs16091555.

de' Michieli Vitturi, M., T. Esposti Ongaro, G. Lari and A. Aravena (2019). IMEX_SfloW2D 1.0: a depth-averaged numerical flow model for pyroclastic avalanches, Geosci. Model Dev., 12, 1, 581-595, doi:10.5194/gmd-12-581-2019.

de' Michieli Vitturi, M., T. Esposti Ongaro and S. Engwell (2023). IMEX_SfloW2D v2: a depth-averaged numerical flow model for volcanic gas-particle flows over complex topographies and water, Geosci. Model Dev., 16, 21, 6309-6336, doi:10.5194/gmd-16-6309-2023.

Di Roberto, A., A. Bertagnini, M. Pompilio and M. Bisson (2014). Pyroclastic density currents at Stromboli volcano (Aeolian Islands, Italy): a case study of the 1930 eruption, Bull. Volcanol., 76, 6, doi:10.1007/s00445-014-0827-5.

Druitt, T. H. (1992). Emplacement of the 18 May 1980 lateral blast deposit ENE of Mount St. Helens, Washington, Bull. Volcanol., 54, 7, 554-572, doi:10.1007/bf00569940.

Esposti Ongaro, T., M. Cerminara, S. J. Charbonnier, G. Lube et al. (2020). A framework for validation and benchmarking of pyroclastic current models, Bull. Volcanol., 82, 6, doi:10.1007/s00445-020-01388-2.

Ferlito, C., M. Viccaro, E. Nicotra and R. Cristofolini (2010). Relationship between the flank sliding of the South East Crater (Mt. Etna, Italy) and the paroxysmal event of November 16, 2006, Bull. Volcanol., 72, 10, 1179-1190, doi:10.1007/s00445-010-0384-5.

Ganci, G., A. Cappello and M. Neri (2022). Data Fusion for Satellite-Derived Earth Surface: The 2021 Topographic Map of Etna Volcano, Remote Sens., 2023, 15, 198, doi:10.3390/rs15010198.

Ganci, G., G. Bilotta, F. Zuccarello, S. Calvari et al. (2023). A Multi-Sensor Satellite Approach to Characterize the Volcanic Deposits Emitted during Etna's Lava Fountaining: The 2020-2022 Study Case, Remote Sen., 15, 4, 916, doi:10.3390/rs15040916.

Giuffrida, M., M. Cardone, F. Zuccarello and M. Viccaro (2023). Etna 2011-2022: Discoveries from a decade of activity at the volcano, Earth Sci. Rev., 245, 104563, doi:10.1016/j.earscirev.2023.104563.

Gueugneau, V., K. Kelfoun, O. Roche and L. Chupin (2017). Effects of pore pressure in pyroclastic flows: Numerical simulation and experimental validation, Geophys. Res. Lett., 44, 5, 2194-2202, doi:10.1002/2017gl072591.

INGV-OE (2022a). Bollettino Settimanale sul monitoraggio vulcanico, geochimico e sismico del vulcano Etna del 6/05/2022-22/05/2022, Rep. N° 21/2022, https://www.ct.ingv.it/index.php/monitoraggio-e-sorveglianza/prodotti-del-monitoraggio/bollettini-settimanali-multidisciplinari/642-bollettino-Settimanale-sul-monitoraggio-vulcanico-geochimico-e-sismico-del-vulcano-Etna-del-2022-05-24/file.

INGV-OE (2022b). Bollettino Settimanale sul monitoraggio vulcanico, geochimico e sismico del vulcano Etna del 7/02/2022-13/02/2022, Rep. N° 07/2022, https://www.ct.ingv.it/index.php/monitoraggio-e-sorveglianza/prodotti-del-monitoraggio/bollettini-settimanali-multidisciplinari/601-bollettino-settimanale-sul-monitoraggio-vulcanico-geochimico-e-sismico-del-vulcano-Etna-del-2022-02-15/file.

Lube, G., E. C. P. Breard, J. Jones, L. Fullard et al. (2019). Generation of air lubrication within pyroclastic density currents, Nat. Geosci., 12, 5, 381-386, doi:10.1038/s41561-019-0338-2.

McEwen, A. S. and M. C. Malin (1989). Dynamics of Mount St. Helens' 1980 pyroclastic flows, rockslide-avalanche, lahars, and blast, J. Volcanol. Geotherm. Res., 37, 3-4, 205-231, doi:10.1016/0377-0273(89)90080-2.

Norini, G., E. De Beni, D. Andronico, M. Polacci et al. (2009). The 16 November 2006 flank collapse of the southeast crater at Mount Etna, Italy: study of the deposit and hazard assessment, J. Geophys. Res., 114, B02204, doi:10.1029/2008JB005779.

Pareschi, L. and G. Russo (2005). Implicit-explicit Runge-Kutta schemes and applications to hyperbolic systems with relaxation, J. Sci.Comput., 25, 129-155, doi:10.1007/s10915-004-4636-4.

Pudasaini, S. P. and K. Hutter (2007). Avalanche dynamics: dynamics of rapid flows of dense granular avalanches, Springer Science & Business Media, 602, doi:10.1007/978-3-540-32687-8.

Risica, G., M. Rosi, M. Pistolesi, F. Speranza et al. (2022). Deposit-Derived Block-and-Ash Flows: The Hazard Posed by Perched Temporary Tephra Accumulations on Volcanoes; 2018 Fuego Disaster, Guatemala, J. Geophys. Res. Solid Earth, 127, 6, doi:10.1029/2021jb023699.

Roche, O. (2012). Depositional processes and gas pore pressure in pyroclastic flows: an experimental perspective, Bull. Volcanol., 74, 1807-1820, doi:10.1007/s00445-012-0639-4.

Sparks, R. S. J. and G. P. L. Walker (1977). The significance of vitric-enriched air-fall ashes associated with crystal-enriched ignimbrites, J. Volcanol. Geotherm. Res., 2, 4, 329-341, doi:10.1016/0377-0273(77)90019-1.

Sulpizio, R. and P. Dellino (2008). Sedimentology, depositional mechanisms and pulsating behaviour of pyroclastic density currents, in Caldera volcanism, developments in volcanology J. Gottsmann and J. Marti (Eds), Elsevier, Amsterdam, 10, 57-96, doi:10.1016/S1871-644X(07)00002-2.

Wilson, C. J. N. and B. F. Houghton (2000). Pyroclasts transport and deposition, in Encyclopedia of Volcanoes H. Sigurdsson (Ed.), Academic Press, San Diego, CA, 545-554.

Zuccarello, F., G. Bilotta, A. Cappello, M. de' Michieli Vitturi et al. (2024). The astonishing paroxysmal episode of 10 February 2022 at Mt. Etna: Lava flow and pyroclastic avalanche hazard assessment through numerical modeling, AIP Conf. Proc., 3094, 1, 330005, doi:10.1063/5.0211793.

Zuccarello, F., D. Andronico, P. Del Carlo, M. de' Michieli Vitturi et al. (submitted). Unraveling the trigger mechanism and propagation dynamics of pyroclastic density currents in basaltic volcanoes, Nat. Commun.

***CORRESPONDING AUTHOR: Francesco ZUCCARELLO**,
Istituto Nazionale di Geofisica e Vulcanologia, Osservatorio Etneo – Sezione di Catania, Catania, Italy
e-mail: francesco.zuccarello@ingv.it